Shear-Induced Crystallization in Blends of Model Linear and Long-Chain Branched Hydrogenated Polybutadienes

Ellen L. Heeley,*,† Christine M. Fernyhough,‡ Richard S. Graham,§ Peter D. Olmsted,§ Nathanael J. Inkson,§ John Embery,§ David J. Groves,§ Tom C. B. McLeish,§ Ariana C. Morgovan,‡ Florian Meneau,|| Wim Bras,⊥ and Anthony J. Ryan‡

Department of Chemistry, The Open University, Walton Hall, Milton Keynes MK7 6AA, United Kingdom, The Polymer Centre, Department of Chemistry, University of Sheffield, Sheffield S3 7HF, United Kingdom, Polymers and Complex Fluids Group, School of Physics & Astronomy, University of Leeds, Leeds LS2 9JT, United Kingdom, Synchrotron Soleil, L'Orme des Merisiers, B.P. 48 Saint Aubin, 91192 Gif sur Yvette Cedex, France, and Netherlands Organization for Scientific Research (NWO), DUBBLE-CRG/ESRF, B.P. 220, F-38043 Grenoble Cedex, France

Received March 21, 2006; Revised Manuscript Received May 25, 2006

ABSTRACT: Quiescent and shear-induced crystallizations were performed on several well-defined linear monodisperse hydrogenated polybutadiene blends with a high-molecular-weight long-chain branched (LCB) comb-shaped additive. The connection between microscopic molecular motion and crystallization kinetics has been quantitatively studied with respect to the formation of either isotropic or oriented shish kebab crystal morphology using time-resolved X-ray scattering techniques. Using a constant preshear rate, the addition of small amounts of LCB combs to the sample blends, at concentrations below and just above the overlap concentration c^*, has significantly increased the crystallization rates compared to quiescent conditions. However, only one blend showed the formation of an oriented shish kebab morphology. Also, for these model blends, the transition between isotropic and oriented crystals occurs quite sharply between 5 and 10%, which is around c^*. We explain these data by using a shish formation mechanism in which, to form shish kebabs, the combs must be mutually overlapping and the comb Weissenberg number must be in the strong stretch regime.

1. Introduction

It is well established that the crystallization of polymer melts can be drastically accelerated by bulk deformation.[1,2] Enhanced crystallization arises from rapid nucleation of many small crystallites, followed by subsequent growth of crystalline material around these nucleation sites. The working hypothesis[2−8] is that deformation leads to rapid homogeneous nucleation during flow, in contrast to the sporadic slow nucleation in quiescent melts. Growth then proceeds centered on these established nucleation sites. Short-term shearing is an experimental protocol that is designed to separate the processes of nucleation and growth. In this procedure, the melt is quenched to the desired temperature and then subjected to a shear pulse of duration much smaller than the typical crystallization time. As the period of deformation is short, negligible growth occurs during the flow and so the influence of flow on the nucleation process can be isolated. This principle was strikingly demonstrated by Stadlbauer et al.[3] who observed homogeneously spaced and equally sized spherulites in polarized light micrographs of an isotactic polypropylene (iPP) melt after a short-term extensional deformation. This is a strong confirmation that the spherulites result from sudden simultaneous nucleation during the flow.

Flow-induced nucleation can be connected to chain stretching due to the flow. The flow distorts chains from their equilibrium, coiled conformations, moving them closer to chain configurations found in crystalline polymers. Thus, the flow breaks down both the entropic and kinetic barriers to nucleation. The degree of chain stretching is also believed to have a strong influence over the type of nucleation. Two possibilities are commonly observed: pointlike nuclei, from which spherulites grow, and oriented threadlike nuclei (shish) from which the so-called shish kebab structure grows.[1] Moderate chain stretching is expected to produce enhanced pointlike nucleation, whereas stronger stretching is thought to lead to threadlike nuclei.[4−6] The striking qualitative difference between these two crystal morphologies can readily be observed via a number of experimental techniques such as X-ray scattering, depolarized light scattering, optical microscopy, and electron microscopy.[3−6]

Chain stretching in a melt can be enhanced by the addition of a high-molecular-weight (HM_w) homopolymer additive.[7,8] The longer relaxation time of the HM_w material means that these chains can accumulate stretch at deformation rates that are accessible in well-controlled experiments. A number of investigations into the effect of blend composition on crystallization behavior have been made, from which similar qualitative trends are beginning to emerge. Seki et al.[7] studied iPP melts and reported a transition to oriented crystals at sufficiently high shear rates, provided that the high-molecular-weight component concentration was above the threshold for long-chain-to-long-chain contact, that is, c^*. Yang et al.[8] also observed oriented growth for HM_w concentrations above c^* in polyethylene blends and also emphasized the role played by the viscosity of the matrix. This onset of oriented growth around c^* suggests that a cooperative mechanism is involved in the formation of shish nuclei. However, an issue in both of the above studies is that the materials are polydisperse in either the matrix, the HM_w

* Corresponding author. E-mail: E.L.Heeley@open.ac.uk.
† Department of Chemistry, The Open University.
‡ The Polymer Centre, Department of Chemistry, University of Sheffield.
§ Polymers and Complex Fluids Group, School of Physics and Astronomy, University of Leeds.
|| Synchrotron Soleil.
⊥ Netherlands Organization for Scientific Research (NWO), DUBBLE-CRG/ESRF.

10.1021/ma0606307 CCC: $33.50
Published on Web 06/30/2006

material, or both. These typical industrial materials have polydispersities with a significant HM_w tail, which makes it difficult to define the overlap concentration because the HM_w tail of the matrix intermingles with the HM_w additive. Furthermore, molecular relaxation times cannot be clearly defined because polydisperse materials have a spectrum of time scales. As a consequence, the connection between microscopic molecular motion and crystallization phenomena is obfuscated.

In this paper, we investigate this issue quantitatively by studying blends of well-defined monodisperse samples of hydrogenated polybutadienes. Long-chain branched comb molecules were chosen as additives because their very long relaxation times allow nonlinear flows to be achieved under well-controlled conditions. We have performed a series of crystallization experiments in which the melts were subjected to a pulse of preshear after cooling to the chosen crystallization temperature and the crystallization rates compared with those under isothermal, quiescent conditions. Crystallization was followed using time-resolved X-ray scattering, which also gave information about the orientation of crystallites. From a molecular rheology model, we calculated the melt relaxation times of our comb and blended samples and confirm these time scales with linear rheological measurements. Finally, we explain our results with a simple picture of how relaxation times and HM_w concentration influence the nucleation, kinetics, and final morphology of the polymer sample.

2. Theoretical Background

By investigating blends of well-defined monodisperse samples of hydrogenated polybutadienes, we observe the flow-induced crystallization of materials whose dynamics under flow are understood, in detail, through molecular theory. For the matrix material, we have chosen entangled linear chains of moderate length (either 15 or 50 kg mol^{-1}), and for the high-molecular-weight additives, we use a model comb polymer with a backbone of 50 kg mol^{-1} and branch length of 15 kg mol^{-1}. The addition of long-chain branching is known to increase relaxation times by orders of magnitude, allowing chain stretching at lower flow rates, so our blends have a very wide separation in the relaxation times between the branched and linear components. Four distinct blends were prepared, using two different length linear chains (15 and 50 kg mol^{-1}, respectively) with combs blended at concentrations of 5 and 10% (see Table 2). These blends allow us to systematically investigate the effect of comb concentration and relaxation time on flow-induced crystallization.

The degree of comb overlap in our comb−linear blends potentially affects the flow-induced crystal morphology, and comb−comb entanglements may affect the combs' relaxation processes. In particular, we are interested in mutual contact between segments of chain that are stretched by the flow. In Appendix A, we demonstrate that the comb backbones are the only segments that can be stretched under our flow conditions. Thus, we must compute the degree of comb overlap by only considering the backbones. To calculate the overlap concentration, c^*, for comb−comb contact, we require the equilibrium dimensions of the combs. Crist et al.[9] used small-angle neutron scattering to measure the radius of gyration, R_g, of a range of linear hydrogenated polybutadienes, and we use their expression $(R_g/\text{Å} = 0.5\,(M_w/(\text{g mol}^{-1}))^{1/2})$ to obtain a backbone radius of gyration of $R_g \approx 116$ Å for the comb. From the formula,

$$c^* \approx \frac{M_w}{R_g^{\,3} N_A \rho} \tag{1}$$

Table 1. Molecular Parameters for the Hydrogenated Polybutadiene Comb and Linear Species

polymer	M_n/g mol^{-1}	M_w/g mol^{-1}	polydispersity (M_w/M_n)
15K linear	16 800	18 100	1.08
50K linear	46 100	50 000	1.09
Comb[a]	129 600	140 100	1.08

[a] The comb was determined to have an average of 5.5 randomly placed branches of a molecular mass of 15 100 g/mol^{-1} on a backbone of 55 800 g/mol^{-1}.

where c^* is expressed as a volume fraction, ρ is the melt density, and N_A is Avogadro's number, we estimate $c^* \approx 0.06 = 6\%$. We note that chain overlap occurs gradually with increasing concentration, and so there is some uncertainty in quantitatively defining the overlap concentration, meaning that c^* can only be estimated. Additional prefactors have been used in expressions for c^*, such as of $4\pi/3$ to account for the spherical shape of the coiled chains. We exclude any such prefactors to reflect the relative uncertainty in defining c^*. Nevertheless, our computed value of c^* provides an indication of the concentration at which overlap will occur. Broadly, we expect little or no significant contact between combs in the 5% blends (blends B15−5 and B50−5) and some contact and even overlap between combs in the 10% blends (blends B15−10 and B50−10).

When considering the chain dynamics, it is important to distinguish between chain overlap and entanglement. Chain entanglement occurs when there is extensive contact between chains that significantly restricts the chain dynamics. However, it is possible for chains to be sufficiently concentrated to overlap without the extensive overlap required to produce entangled dynamics. Given that our most concentrated blends just exceed the overlap concentration, c^*, we conclude that there are no significant comb−comb entanglement in the samples investigated here. In Appendix A, our rheological measurements confirm that the comb dynamics are independent of concentration.

We predict values for the various relaxation times of our blends by using the Doi−Edwards tube theory[10] and confirm these time scales by measuring the linear oscillatory shear data for each of the materials in this study (see Appendix A for details). We use this modeling to provide various relaxation times and to classify the flow regimes experienced by the polymer melts prior to crystallization. From these calculations, we conclude that, under the shear conditions used throughout this investigation ($\dot{\gamma} = 100\ s^{-1}$), no significant deformation of the linear matrix will occur; however, moderately strong stretching will occur in the comb blends with the 15 k matrix and very strong stretching in the combs in the 50 k matrix. We anticipate that any enhanced nucleation will result from the dynamics of the combs, with no contribution from the linear matrix material. Furthermore, the comb dynamics are unaffected by the change in concentration from 5 to 10% because the combs are not self-entangled. Thus, the degree of stretch is expected to be the same between these blends, while the density of potential nucleation sites will double, allowing us to investigate changes in crystallization rate and morphology as the density of potential flow-induced nucleation sites is varied.

3. Experimental Methods

3.1. Synthesis and Materials. The materials were synthesized using anionic polymerization techniques. The synthesis and characterization of hydrogenated polybutadiene (hPBd) combs and linear samples has been described in detail elsewhere.[11] Table 1, summarizes the molecular weights of the hPBd samples used herein. The blends were made by mixing the appropriate amount of comb

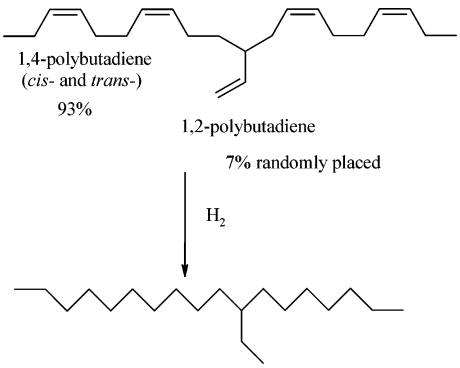

Figure 1. Schematic of short-chained branching in the PBds once hydrogenated.

Table 2. Composition of the Hydrogenated Polybutadiene Comb−Linear Blends

blend	composition (w/w)
B15−5	95% 15 K linear +5% comb
B15−10	90% 15 K linear +10% comb
B50−5	95% 50 K linear +5% comb
B50−10	90% 50 K linear +10% comb

Table 3. DSC Melting and Crystallization Temperatures for hPBd Homopolymers and Blends

sample	T_m/°C	T_c/°C
15 K linear	113	93
50 K linear	111	86
comb	104	79
B15−10	108	94
B50−10	108	87
B50−5	107	89
B15−5	108	94

and linear hydrogenated polybutadiene together and dissolving in toluene at 90 °C at a concentration of 2% w/v. Once the polymers had completely dissolved, the blend was precipitated in methanol. The blends were then filtered and dried under vacuum. The blend compositions are listed in Table 2.

The anionic polymerization of butadiene in a hydrocarbon solvent such as hexane results in a predominately 1,4-enchained structure; however, 7% of the monomer undergoes a 1,2-Michael addition purely at random during the polymerization. Short-chain ethyl branches are produced when the 1,2-enchained units are hydrogenated, as shown in Figure 1. The linear hPBds are therefore analogous to a polyethylene-*co*-butene whereby ethyl groups are homogeneously distributed along a polyethylene chain with an average frequency of one ethyl group for every 55 CH_2 repeat units. The reduction in final crystallinity is a known consequence of the distribution of ethyl branches in such samples. Here, they can effectively expand the crystalline unit cell by partial inclusion into the crystal, hence causing defects and lowering the bulk crystallinity.[12,13] However, often the ethyl branches will be completely excluded from the crystal into the amorphous or transition phase[14] as are any noncrystallizable longer branches, causing a stronger depression of crystallinity.[12]

Melting and crystallization temperatures for all homopolymer and blended hPBd samples were determined using a Perkin-Elmer Pyris 1 DSC calibrated by the melting points of indium and cyclohexane standards. Samples of mass 5−10 mg, in aluminum pans, were subjected to heating and cooling ramps from 25 to 140 °C at 10 °C min^{-1}. Melting and crystallization temperatures were obtained from the peaks of the endotherms and exotherms, during programmed heating and cooling regimes, respectively, using the Pyris DSC software, and are reported in Table 3.

3.2. Rheological Measurements. The relaxation times of each of the materials were characterized by linear oscillatory shear measurements on a Rheometrics ARES rotational rheometer under a nitrogen atmosphere. Polymer samples were vacuum-dried, compacted using a piston and cylinder as necessary, and then premolded to a suitable thickness and geometry using a template and platen press. Typical molding press temperatures were up to 180 °C, depending on molecular weight. The linear viscoelastic modulus, $G(\omega)$, was measured using either 10 mm or 25 mm diameter parallel plates or a 10 mm diameter cone and plate with 2° or 5° included angle. Master curves were produced from time−temperature superposition of frequency sweep data between 110 and 170 °C by using WLF parameters consistent with those reported in Pearson et al.[15] The temperature range was limited to temperatures above the crystallization temperature (see Table 3), restricting measurements to the low-frequency regime. For the pure combs and comb−linear blends, some other features of the relaxation spectrum could be measured, but only the terminal behavior was accessible for the pure linear samples. To resolve the problems of low measured torques in the low-frequency regime, we used unusually large strains of up to 50%. Linear response was assured, despite these high strains, provided the frequency was below the melt terminal time.

3.3. X-ray Scattering Measurements. Time-resolved quiescent and shear small-angle X-ray scattering (SAXS) experiments were performed at the Dubble GRG BM26B beam line of the European Synchrotron Radiation Facility (ESRF), Grenoble, France. The ESRF beam line optics and construction are detailed elsewhere.[16] The ESRF Dubble beam line operates at variable wavelengths, and a wavelength $\lambda = 1.03$ Å was used in this investigation throughout. Either a one-dimensional (1D) or two-dimensional (2D) multiwire gas-filled SAXS detector was situated 8 m from the sample position and instrumentation, and a vacuum chamber is placed between the sample and SAXS detector to reduce air scattering and absorption. The scattering vector axis, q, of the SAXS patterns were all calibrated using an oriented sample of dry rat-tail collagen.

3.3.1. Quiescent Crystallization. Disk-shaped samples (~1 mm thickness, ~8 mm diameter) were contained in aluminum DSC pans (TA Instruments) fitted with mica windows (~25 μm thickness, ~7 mm diameter).[17] The pans were placed into a Linkam DSC, whose design and calibration has been previously reported.[18] Samples were heated from 25 to 150 °C at a rate of 20 °C min^{-1} and held at this temperature for 5 min. The samples were subsequently quenched at 50 °C min^{-1} to the isothermal, quiescent crystallization temperature T_i, and held for up to several hours depending upon T_i in the range $T_c < T_i < T_m$, where T_c is the crystallization maximum during cooling at 20 °C min^{-1}, and T_m is the melting maximum heating at 20 °C min^{-1}. Time-resolved SAXS measurements using a 1D SAXS detector system, were obtained for each quiescent crystallization temperature. The X-ray data acquisition was collected at 8 s per frame, with each frame separated by 10 μs wait time.

3.3.2. Shear-Induced Crystallization. A Linkam CSS450 shear cell, in which the optical quartz windows had been replaced by stainless steel inserts with an X-ray aperture of Kapton foil (100 μm), was used to study shear-induced crystallization. A similar X-ray setup for the Linkam CSS450 is documented elsewhere.[19,20] A 1.5 g sample of homopolymer or blend was placed in the shear cell, and the lid and base gap was set to 500 μm. All samples were heated to a temperature of 150 °C at a rate of 10 °C min^{-1}, held for 5 min, and then quenched at 30 °C min^{-1} to the crystallization temperature, T_i. Once T_i had been reached, a pulse of shear of 500 shear units, was given to the sample (100 $s^{-1} \times 5$ s), and then the sample was left to crystallize quiescently at this temperature. Each frame of time-resolved 2D SAXS measurements was recorded over 5 s, with a 10 μs wait time between frames, until the crystallization process was complete.

4. Data Analysis

SAXS data were corrected for background scattering by subtracting contributions from the camera, hot stage, and the homogeneous hPBd melt, and corrected for any detector spatial distortion. Sample thickness and transmission was accommodated by using signals from two parallel-plate ionization chambers placed before and after the sample cell.

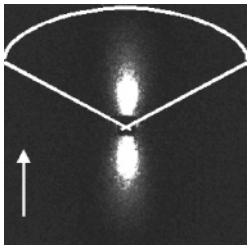

Figure 2. Example of a sector integration of a 2D SAXS pattern. The white lines indicate the typical sector used (center 256, 256; constant start and finish angles 20°, 160°; radius of 248 pixels). The arrow indicates shear direction and meridian.

The quiescent 1D SAXS crystallization data were reduced to intensity I, as a function of scattering vector $q = (4\pi \sin \theta/\lambda)$ where θ is the scattering angle, using the CCP13 software program, XOTOKO.[21] The relative invariant Q_s derived from the SAXS data[22] was used to follow the development of crystallization,

$$Q_S(t) = \int_0^\infty q^2 I(q,t)\, dq \approx \int_{q_1}^{q_2} q^2 I(q,t)\, dq \qquad (2)$$

The shear-induced 2D SAXS data were reduced to an effective 1D intensity, $I_{eff}(q,t)$, by sector averaging symmetrically around the meridian by a given angle, a fixed radius q, using the CCP13 software program BSL.[21] Figure 2 shows an example of the sector integration region taken on a typical SAXS pattern. From this sector integration, the relative invariant $Q_s(t)$ was obtained for the crystallization process with respect to time using the XOTOKO program. The characteristic long period, L_p, was determined from the SAXS data by using a one-dimensional correlation function approach[23−25] described later.

Figure 3 shows a normalized plot of quiescent and shear-induced crystallization curves for the pure comb sample obtained from the invariant calculation. The half-time ($t_{1/2}$) of the crystallization process is indicated on the graph. This value represents the time to reach 50% conversion to the final full crystallinity of that sample at a particular crystallization temperature.

From the SAXS-normalized invariant data, Avrami plots[26] were obtained for sheared and quiescent crystallizations. The Avrami model takes the general form

$$1 - X_s = e^{-kt^n} \qquad (3)$$

where $X_s(t) = Q_s(t)/Q_s(\infty)$ is the crystallinity, k is the rate constant of the crystallization process, and n is the Avrami exponent, which provides information about the overall crystallization rate and dimension of the growing crystalline material. This model assumes that the nuclei for the "growth unit" (e.g., spherulites), are fixed in time, and it allows for the eventual impingement of the growth unit, which limits further expansion. To extract the values of n and k from the SAXS invariant data,

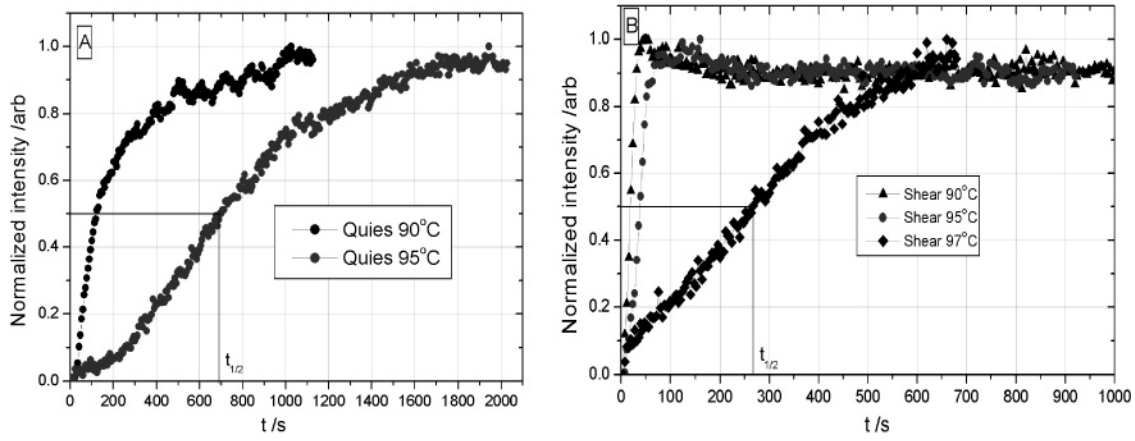

Figure 3. (A) Quiescent and (B) shear-induced crystallization curves for the pure comb sample at several temperatures, shown by the development of the invariant $Q_s(t)$, from the SAXS data.

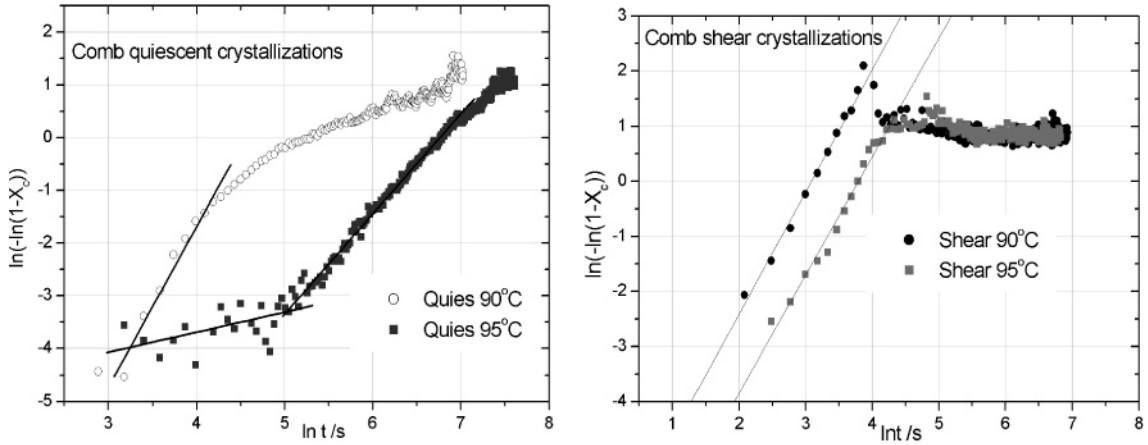

Figure 4. Avrami plots (eq 4) from the crystallization curves for the comb sample at 90 and 95 °C, under quiescent and shear conditions, respectively. In the linear region, the slope and the $t = 1$ intercept give the Avrami exponent n and the rate constant ln k, respectively. The quiescent crystallization at 95 °C suggests two regions of growth (see main text).

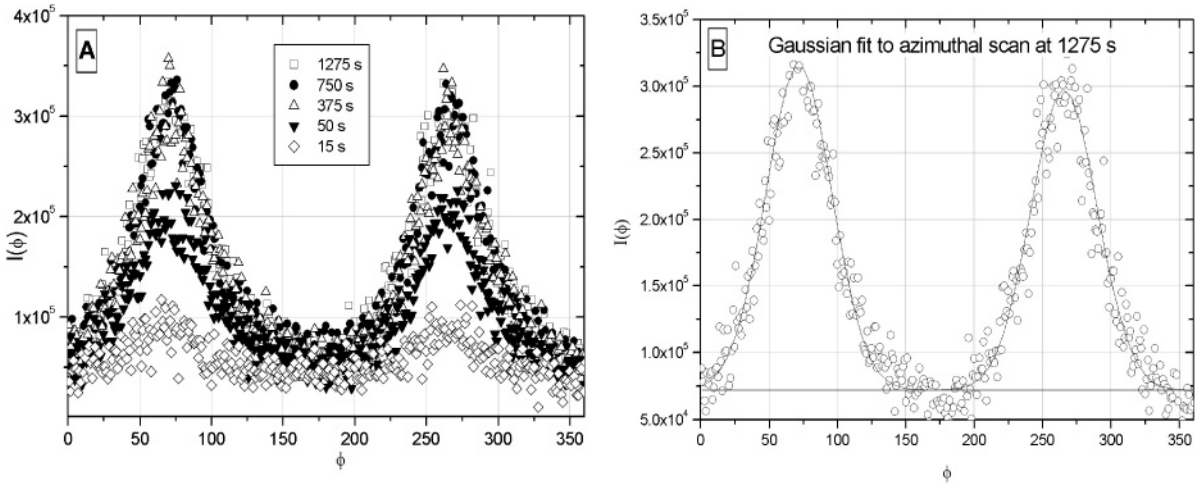

Figure 5. (a) Intensity at q^* vs azimuthal angle (ϕ) from the oriented 2D SAXS data of the presheared pure comb sample at 90 °C with respect to time. (B) Example of a Gaussian fit to the final frame of data used to obtain the full width at half-maximum to calculate the degree of orientation.

Table 4. Avrami Exponent *n* for Various Types of Nucleation and Free Growth

Avrami exponent, *n*	nucleation type and growth unit
1	fibrils from instantaneous nuclei
2	fibrils from sporadic nuclei or disks from instantaneous nuclei
3	disk from sporadic nuclei or spherulites from instantaneous nuclei
4	spherulites from sporadic nuclei
6	sheaf from sporadic nuclei

the double logarithmic form of the Avrami equation is used:

$$\ln(-\ln[X_s(t)]) = n \ln t + \ln k \quad (4)$$

Figure 4 shows examples of the Avarmi plots for the pure comb sample at various temperatures under quiescent and shear conditions. The Avrami exponent increases as the "dimensionality" of the growth unit increases. Values of *n*, and the type of nucleation process involved, are given in Table 4.

The comb sample has an Avrami exponent between 2 and 3 when crystallizing under shear or quiescent conditions (Figure 4), which could indicate a low dimensional growth unit. It should be noted that, for the quiescent crystallization at 95 °C, a feature is seen in the Avrami plot indicating, apparently, two regions of growth. From Figure 4, these two regions can be fitted with distinctly different Avrami exponents, both with lines originating from $t = 0$, corresponding to the time at which the crystallization temperature was reached. The first slope may be an artifact of the low scattering signal during the early stages of the crystallization. However it can be misleading to disregard data that represent early stages of crystallization.[27] Alternatively, this region may indicate a rapid but very low dimensional growth process (Avrami exponent ~0.3), which occurs at the early stage, then is subsequently overwhelmed by the slower higher dimensional growth that is seen at the later stage (Avrami exponent of 3) of the crystallization.

Deviations from the Avrami model, such as the noninteger *n* or nonlinear plots that we find, are often attributed to the simultaneous or consecutive of growth of the crystalline units[28−30] and the other inappropriate assumptions in the Avrami model. Nevertheless, the Avrami model allows us to assess how far from these idealized situations the crystallization experiments are.

To obtain an estimate of the relative orientation distribution of crystallites postshear (where samples showed clear anisotropy in the 2D SAXS patterns), the angular variation of intensity, $I(q^*, \phi)$, was examined at fixed radius, q^*. The value of q^* was chosen as the radius at which the peak intensity occurs. To obtain each $I(q^*, \phi)$ value, the SAXS data were averaged over a small region centered on (q^*, ϕ) by using the BSL program.[21] Typical data, covering the full 360° range in ϕ, are shown in Figure 5. The final full width at half-maximum (fwhm)[6] was obtained as an average of the two fitted peaks by using a Gaussian peak shape.

Finally, the SAXS data were analyzed using a one-dimensional correlation function to derive several structural parameters associated with the crystals. The cosine Fourier transform of the SAXS intensity data was calculated, and the resulting curve is interpreted to extract parameters that describe a model of lamellar microstructure.[31−33] These parameters include the long period or lamellar repeat distance, crystal and amorphous layer thicknesses, and estimated volume crystallinity. The one-dimensional correlation function is expressed as:

$$\gamma_1(R) = \frac{1}{Q_s} \int_0^\infty I(q) q^2 \cos(qR)\, dq \quad (5)$$

where $I(q)$ is the scattering intensity. To perform the integration, the non-Lorentz-corrected SAXS data were extrapolated to $q \rightarrow \infty$ according to Porod's law,[34] $I \sim q^{-4}$, and to $q \rightarrow 0$ according to the Guinier model,[31] $I \sim A + Bq^2$.

The extrapolations and generation of the one-dimensional correlation function from the SAXS data was performed using a set of purpose-written programs, known collectively as Corfunc.[35,36] As an example, the correlation function for the final frame of data from the comb sample sheared at 90 °C, along with the interpretation of its features in terms of an ideal two-phase lamellar morphology, is given in Figure 6. Correlation functions were performed on all the final data frames of the quiescent and shear crystallizations. The structural parameters extracted included the long period (L_p), hard (H_b), and soft (S_b) block thicknesses relating to the crystalline and amorphous stacking units, respectively, and the percent of bulk crystallinity. For the comb sample, correlation function analysis was performed on the complete time-resolved SAXS data, giving the changes in derived parameters with respect to time during the crystallization process.

5. Results and Discussion

5.1. DSC Analysis. The initial DSC analysis of the homopolymer and blended samples (Table 3) shows that the pure

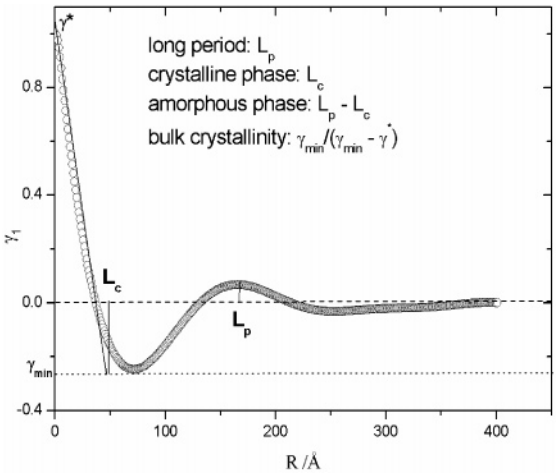

Figure 6. One-dimensional correlation function, calculated from Corfunc, for the final frame of data from the presheared pure comb sample crystallized at 90 °C, along with the interpretation of its features in terms of an ideal two-phase lamellar morphology.

comb sample has slightly reduced melt and crystallization temperatures compared with those of the pure linear homopolymers, as would be expected due to the long-chain branching of the combs hindering crystallization.[13,14] The blended samples also showed slight reductions in T_m compared with the homopolymers, again to be expected upon addition of the comb material.

5.2. Orientation and SAXS. From the 2D SAXS data, certain blends and the comb homopolymer clearly showed some degree of orientation in the structure, which could be due to oriented lamellar stacking or "shish kebab" structures. Figure 7 gives some basic examples of commonly observed oriented SAXS patterns[37] and their corresponding arrangement of crystalline and amorphous units. These simple patterns can be related to the 2D SAXS data obtained here, although often a mixture of structures can be identified.

In Figure 8A, several frames of SAXS data are shown for the shear-induced crystallization of the pure comb sample at 90 °C. In Figure 8B, sector integrations $I(q)$ are given for the final structure following crystallization at 90, 95, and 97 °C. It is clear that, after ∼15 s, an anisotropic scattering pattern begins to develop, with meridional spots corresponding to Figure 7A, indicating the formation of well-defined lamellae stacked perpendicular to the flow direction. Crystallization is nearly completed by ∼60 s, and the correlation function analysis gave the final lamellar and amorphous stacking repeat period L_p as ∼160 Å.

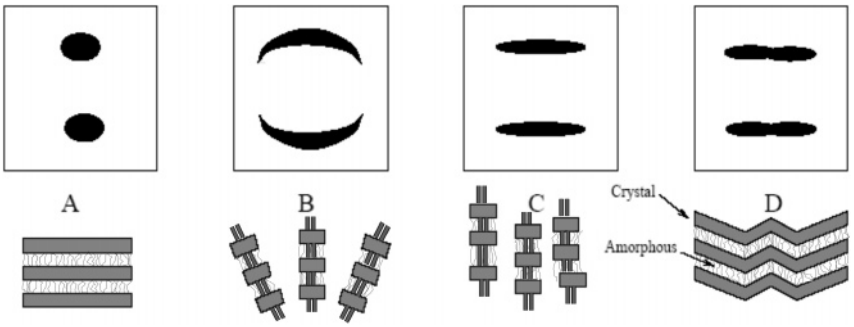

Figure 7. Commonly observed SAXS patterns in oriented polymer samples. (A) Sharp meridional spots: broad parallel lamellae; (B) meridional arc: several orientations of narrow lamellae or "shish kebab" structures; (C) diffuse spots: oriented fibrils with narrow lamellae or "shish kebab" structures; (D) "four point" pattern: herringbone structure (Rober et al.[37]).

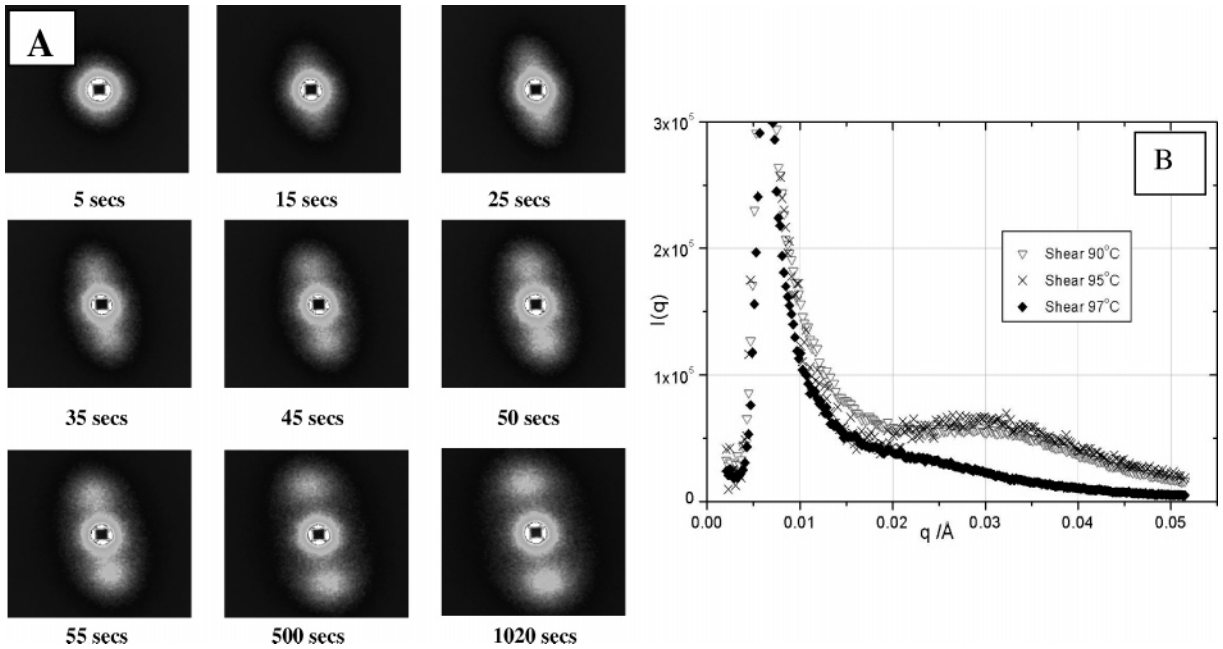

Figure 8. (A) Two-dimensional SAXS patterns observed for shear-induced crystallization of the pure comb sample at 90 °C. The frame rate is 5 s, and the time intervals are given after the cessation of the shear pulse. (B) Corresponding final frame sector integrations $I(q)$, used for determining L_p.

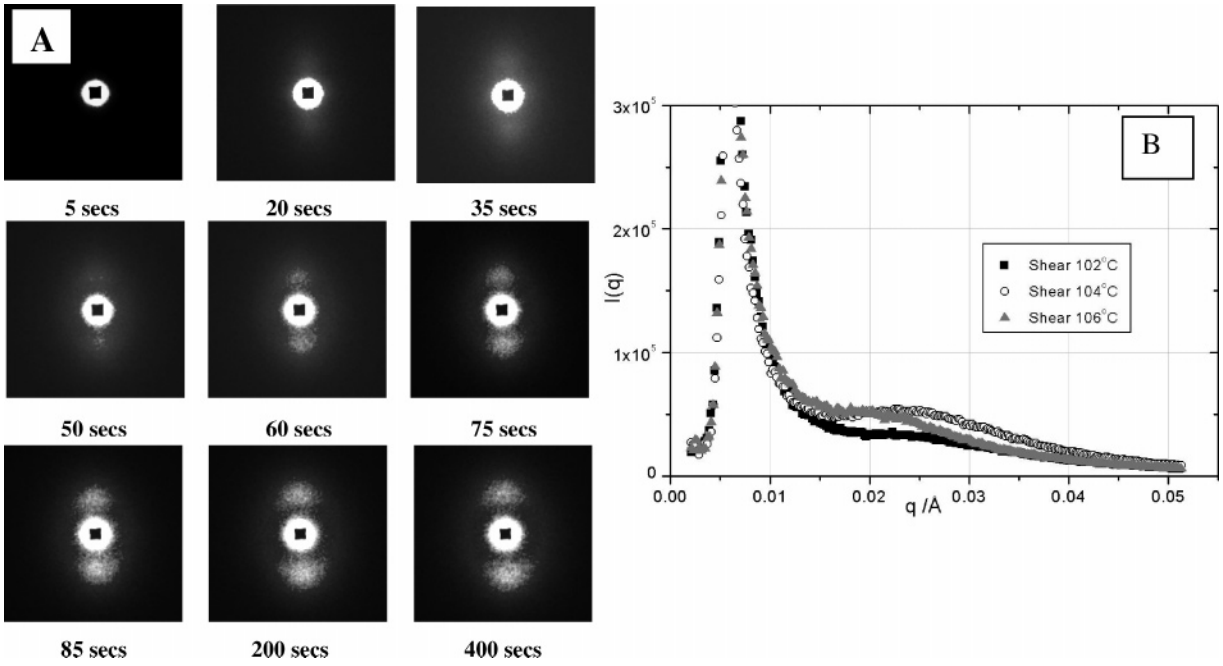

Figure 9. (A) Two-dimensional SAXS patterns observed for shear-induced crystallization of B50−10 at 104 °C. (B) Corresponding final frame sector integrations $I(q)$ used for determining L_p.

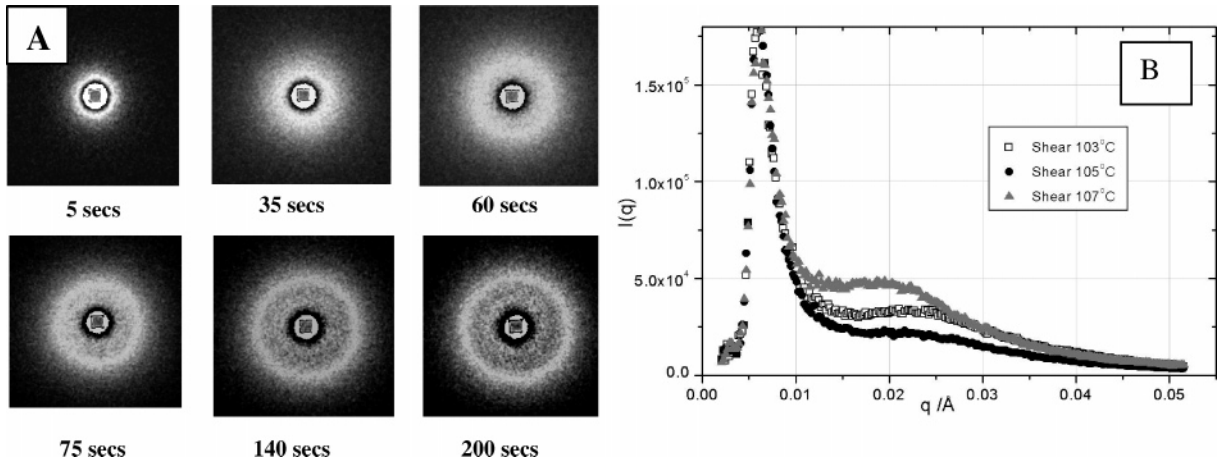

Figure 10. (A) Two-dimensional SAXS patterns observed for shear-induced crystallization of B50−5 at 103 °C. (B) Corresponding final frame $I(q)$ used to determine L_p.

In Figure 9A, similar 2D SAXS patterns show the crystallization of blend B50−10 at 104 °C. In Figure 9B, sector integrations $I(q)$ are given for the final structure following crystallization at 102, 104, and 106 °C. Here, the patterns are somewhat less oriented than those of the pure comb sample. The mixture of diffuse spots and arcs indicates a component of oriented fibril or "shish kebab" structure, while the faint diffuse halo indicates that isotropic lamellae are also present in the final structure. The long period obtained from the correlation function following crystallization at 104 °C is ∼210 Å.

The 2D SAXS data for the more dilute B50−5 blend at 103 °C shows no obvious anisotropy (Figure 10A). The crystallization is complete in ∼2 min, and the isotropic scattering ring indicates a spherulitic lamella structure with a final $L_p \sim 200$ Å. Both the B15−10 and B15−5 blends show similar isotropic, diffuse circular scattering patterns when undergoing shear-induced crystallization.

The width of the scattering peak (fwhm) values are plotted with respect to temperature for the comb and B50−10 samples in Figure 11.

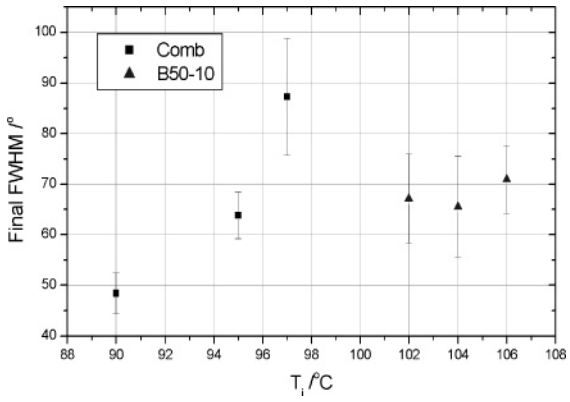

Figure 11. Final peak width (fwhm) for comb and B50−10 samples calculated from the azimuthal scans providing an estimate of crystallite orientation with respect to crystallization temperature.

These were the only two samples that showed any anisotropy in the 2D SAXS patterns, hence an estimation of the degree of orientation is made using the azimuthal scans. Generally, the degree of orientation in both samples is reduced as the

Table 5. Crystal Morphology Parameters from the Correlation Function Analysis on Samples Crystallized Following Shear and under Quiescent Conditions[a]

				hard & soft block thickness/Å: quiescent		hard & soft block thickness/Å: sheared		% bulk crystallinity quiescent (*Qu*)/and sheared (*S*)	
sample	T_i/°C	L_p quiescent/Å	L_p sheared/Å	H_b	S_b	H_b	S_b	*Qu*	*S*
comb	90	300	165	55	245	35	130	17	18
	95	320	170	51	269	35	135	17	17
	97		200			45	155		13
B15−10	101	240		55	185			12	
	103	250		55	195			11	
	105	250	190	50	200	45	145	10	18
	107		210			45	165		17
	109		230			45	185		17
B50−10	100	330		56	274			17	
	102	350	200	52	298	43	157	15	14
	104	380	210	55	325	44	166	10	19
	106	380	220	55	325	46	174	10	15
B50−5	101	320		50	270			17	
	103	370	200	55	315	40	160	16	18
	105	410	200	60	350	40	160	13	16
	107		230			41	190		18
B15−5	105	340	190	55	285	46	144	12	9
	107	370	200	58	312	46	154	11	11

[a] Where parameters are not reported, either the crystallization was not performed at these temperatures (being too high for quiescent condition and too low following shear) or the lamella interpretation of the correlation function analysis failed.

crystallization temperature is increased toward the melt temperature, indicated by an increase in the fwhm. This decrease in orientation is influenced by the chain relaxation, which will increase toward the melt temperature. However, it is difficult to compare the orientation for the blend and comb samples, as the relaxation kinetics will differ greatly due to the influence of matrix material and the comparison at the same temperatures is also not possible. The pure comb sample shows the greatest relative orientation at 90 °C, and it is expected that the relaxation times of the pure comb is longer that that of the same comb molecules in the 50 k linear matrix in blend B50−10. The relative orientation estimation here indicates that the comb and B50−10 samples have an oriented macrostructure after preshearing (at those temperatures investigated). The other blends did not show any relative orientation under the same presheared conditions.

The structural parameters for the final semicrystalline morphology for both the quiescent and sheared samples are summarized in Table 5. The long period L_p generally decreases with decreasing crystallization temperature, indicating greater crystallinity and ordering of lamellae (reduced thickness of the amorphous component). The long period also decreases when the system is sheared independent of the degree of orientation. Only during crystallization of the presheared pure comb sample and B50−10 was there any obvious orientation seen in the 2D SAXS patterns. The decreased L_p can be understood as being due to the insertion and growth of small lamellae or "kebabs" (B50−10) or highly regular stacks of lamellae in the pure comb sample compared with that of the quiescent crystallization. B50−10 does show some diffuse scattering, however, indicating that some lamellae are randomly oriented in the sample also. For the unoriented samples resulting from presheared melts (B50−5, B15−10, and B15−5), the reduction in L_p indicates randomly oriented but more closely packed lamellae/amorphous repeat units compared with similar quiescent quenches.

One feature that is common to both sheared and quiescent crystallizations is that the thickness of the crystalline unit (H_b) of either lamellae or fibril nature is relatively constant at an average of $\sim 50 \pm 10$ Å. This can be attributed to the presence of ethyl groups acting as point defects (approximately every 55 CH_2 repeat units where the average bond length is 1.54 Å), which prevent large crystallites from forming.[38,39] This is also reflected in the average percent of bulk crystallinity, which is below 20% even in the sheared samples. Certainly, the low bulk crystallinity values for the hPBd samples is expected due to the influence of short-chain branching defects and crystallization history. Thus, the reduction in L_p of the crystallized sheared samples is due to the smaller amorphous regions resulting from the insertion of lamellae, but these crystalline units are small and diffuse with low overall bulk crystallinity.

Some values of bulk crystallinity in hPBds have been reported to be as high as ~40%,[13,14] although this is still below the general value for commercial low-density polyethylene (LDPE), which can range between 50 and 60%[28] depending upon thermal and physical treatment. Higher values of crystallinity, compared with those reported here, are mainly due to the differences in thermal and physical treatment of the polymer. The crystallinity values are determined here at the crystallization temperature, which in all cases, are close to the melt temperature. However, the crystallinity is higher if measured at room temperature[14] rather than the elevated temperatures we have used here.

The time-resolved one-dimensional correlation function analysis in Figure 12 shows how the morphology develops in the presheared pure comb sample over a range of temperatures. At the beginning of the crystallization process, the scattering is not yet that of a two-phase lamellar morphology. As the crystallization proceeds, however, such a morphology develops. L_p emerges and then decreases rapidly to a slightly smaller value, a trend also seen in the amorphous and crystalline block phases. The greater long period at higher crystallization temperatures indicates a larger amorphous thickness because the hard block size remains practically constant at ~50 Å. As expected, the total bulk crystallinity increases rapidly during the early stages of the crystallization process and is usually slightly greater in the presheared samples compared to the quiescent cases. Conventionally, lamellar crystal thickening is usually observed during crystallizations in polyethylenes,[40,41] but this is inhibited in the hydrogenated polybutadiene because of their short-chain branching and crystalline point defects and, hence, low bulk crystallinity.[42−44]

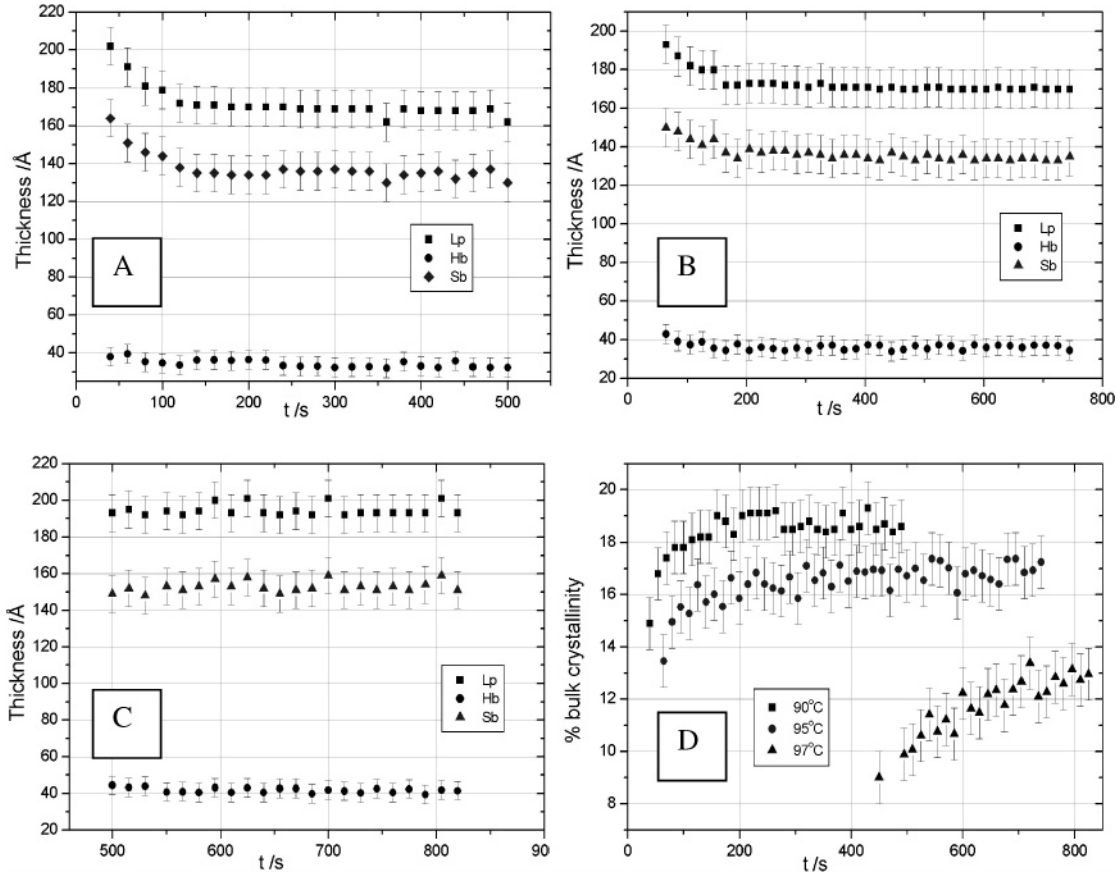

Figure 12. Time dependence of the long period (L_p), lamellae thickness (H_b), and amorphous (S_b) components during the crystallization of the pure comb sample after shear at (A) 90 °C, (B) 95 °C, and (C) 97 °C and (D) change in average bulk crystallinity.

The morphological parameters extracted from the correlation function analysis show simply that, as the crystallization temperature decreases, the overall crystallinity increases and the long period decreases, as expected. Imposing a shear flow on the sample before crystallization tends to increase the overall crystallinity but reduces the periodicity because there are more thin crystals formed that are closer together. The same trends are followed with respect to crystallization temperatures independent of the flow history. The one-dimensional correlation function analysis only provides a correct morphological description for an ideal two-phase lamellar system. While this is entirely appropriate for quiescent crystallizations, the application of an isotropic cosine transform is not formally correct for oriented systems. In many cases,[45−47] however, correlation function analysis has successfully been applied to semicrystalline polymers, where the one-dimensional correlation function from 2D SAXS is used to describe the variation in electron density along the fibril or lamellae stack. Here, we have applied the one-dimensional correlation function analysis to both the anisotropic and isotropic 2D SAXS data to describe the shish kebab or lamellar stacking during crystallization for comparison.

The integrated total intensity was used to assess the time dependence of crystallization. First, the normalized SAXS crystallization curves were plotted and the crystallization half-times ($t_{1/2}$) obtained. These crystallization curves are given in Figure 3 for the pure comb sample and in Figure 13 for the blends. For the quiescent crystallizations in Figure 13, the complete crystallizations are not shown to $t = \infty$, but all $t_{1/2}$ are calculated using the complete crystallization curves.

Table 6 shows the Avrami exponent n, rate constant k, and the crystallization half-times for the cases where data for shear and quiescent crystallization have been obtained at the same temperatures. Unfortunately, Avrami analysis cannot separate the influence of nucleation type from dimensionality of the crystallites. Crystallizations postshear generally show an Avrami exponent lower than that for the corresponding quiescent crystallization, consistent with a shift away from sporadic toward instantaneous nucleation. The sheared crystallizations give $n \leq 2$, which indicates a low two-dimensional growth of a fibril or rod, although no correlation between n and orientation in the SAXS patterns is evident. As the crystallization temperature increases, the value of n generally decreases in quiescent crystallizations but there is no general trend in the sheared data. This implies that the dimensionality of growth is reduced with increasing crystallization temperature for both the presheared and quiescent samples. Interestingly, the lowest Avrami exponent is seen for the blends B15−5 and B15−10, which in some cases is ≤ 1, suggesting a very low dimensional dendritic type of growth unit, which has been identified for lower-molecular-weight branched polyethylenes.[29,30] The Avrami rate constant k is greatly increased from the quiescent crystallizations to the presheared crystallizations, and generally decreases with increasing crystallization temperatures, thus supporting the supposition that shear increases the nucleation kinetics while the crystal growth slows down as the temperature is increased.

Figure 14 presents the crystallization half-times as a function of $1/T$ for both quiescent and shear crystallization of the blends, the pure comb and linear homopolymers. The data fall on straight lines of similar slope, indicating a consistent Arrhenius temperature dependence of the rate of crystal growth. As expected for the blends, the quiescent crystallization is unaffected by the addition of small amounts of combs; the rate is determined by the molecular weight of the matrix and is comparable to that of the pure matrix. The quiescent crystal-

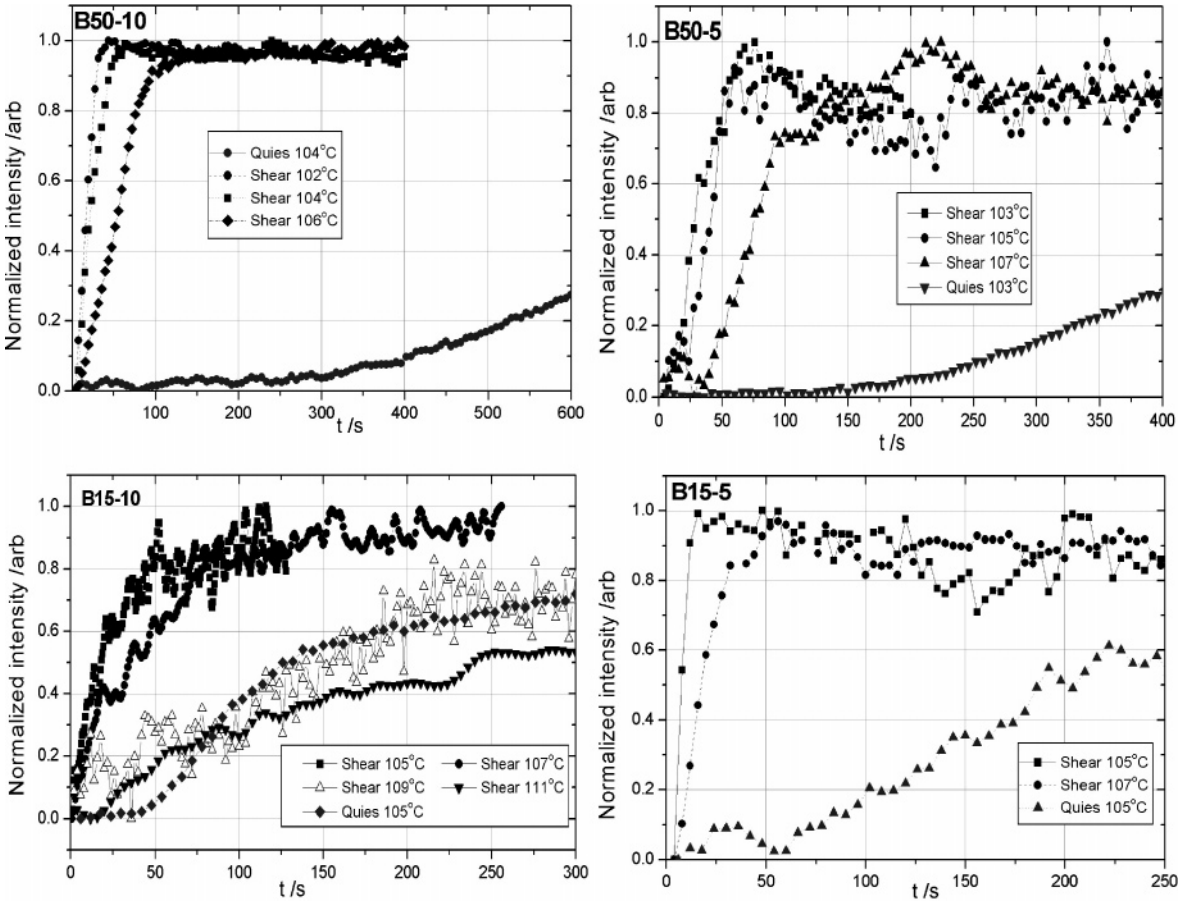

Figure 13. Normalized crystallization curves for presheared and quiescent blends at several temperatures. The data from quiescent samples are only shown over the time range of the sheared crystallizations for comparison, but $t_{1/2}$ is calculated from the entire crystallization.

Table 6. Avrami Analysis and Crystallization Half-Times for Pure Comb and Blend Samples at Temperatures for Which There Is Both Quiescent and Sheared Data

		Avrami exponent n		$\ln k/s^{-1}$		$t_{1/2}$/s	
sample	T_i/°C	quiescent	shear	quiescent	shear	quiescent	shear
comb	90	3.0	2.2	−13.8	−6.9	129	20
	95	1.9	2.1	−12.7	−8.1	708	40
B15−10	105	3.6	0.5	−17.2	−1.7	126	7
	107	2.2	0.8	−13.4	−3.0	420	17
B50−10	102	3.8	2.0	−18.8	−6.0	372	17
	104	3.0	1.9	−18.6	−6.3	864	22
	106	1.6	1.8	−13.0	−7.5	2340	56
B50−5	103	2.7	1.8	−17.1	−6.6	550	90
	105	2.4	2.3	−18.1	−8.7	1445	185
B15−5	105	2.9	0.8	−13.0	−1.1	200	8
	107	3.2	1.6	−18.5	−5.3	457	18

lization of the pure combs is significantly slower than the other materials. In fact, for all materials in the study, the quiescent crystallization half-time follows the same sequence as the bulk relaxation time, as both of these processes are diffusion controlled. For blends B15−5 and B15−10, the half-time of the sheared crystallization roughly halves when the density of combs is doubled. This is consistent with no change in chain dynamics between blends (see Appendix A) and the density of nucleation sites rising in proportion with the comb density. The difference in half-time between blends B50−5 and B50−10 changes more dramatically upon changing the comb concentration from 5 to 10%. The qualitative difference between the final morphology for these two blends means that a direct correlation between the crystallization half-time and comb concentration cannot be made for these blends. The observed shift in half-time, however, is consistent with the significantly larger nucleation area expected for threadlike nuclei when compared with pointlike nuclei. Finally, in each sample, the scaling of the half-time with temperature is the same in the quiescent and sheared experiments, confirming that the growth rate following nucleation is not affected by the shear history.

5.3. Interpretation of the Final Crystal Morphology. Now we relate the crystallization rate and morphology to the relaxation times of the blended combs. In particular, we discuss the connection between flow-induced molecular stretch and enhanced crystallization rate and demonstrate that a specific regime of both shear rate and comb concentration is required to form shish kebabs. To predict the degree of flow-induced chain stretching, we compare the effective relaxation times of the blended combs, computed in Appendix A, to the deformation rate. No stretching occurs in the linear matrixes due to their fast relaxation times and so we can assume that all changes in nucleation and crystallization rates to arise from the combs.

Although samples containing combs had flow-enhanced crystallization rates, only a few had oriented 2D SAXS patterns, which are due to shish kebab formation. To form shish nuclei, the chains must be oriented at the monomer bond level and this level of orientation can only be produced by chain stretching. Two regimes of stretching can be identified based on the chain configuration. In the moderate stretching regime, the contour length of the tube is increased by flow but the chain configurations remain essentially Gaussian, where the degree of bond orientation is low. Conversely, in the strong stretching regime, the contour length is increased to close to its maximum value, the influence of finite extensibility sets in, and the amount of bond orientation is large. It is generally assumed that, to

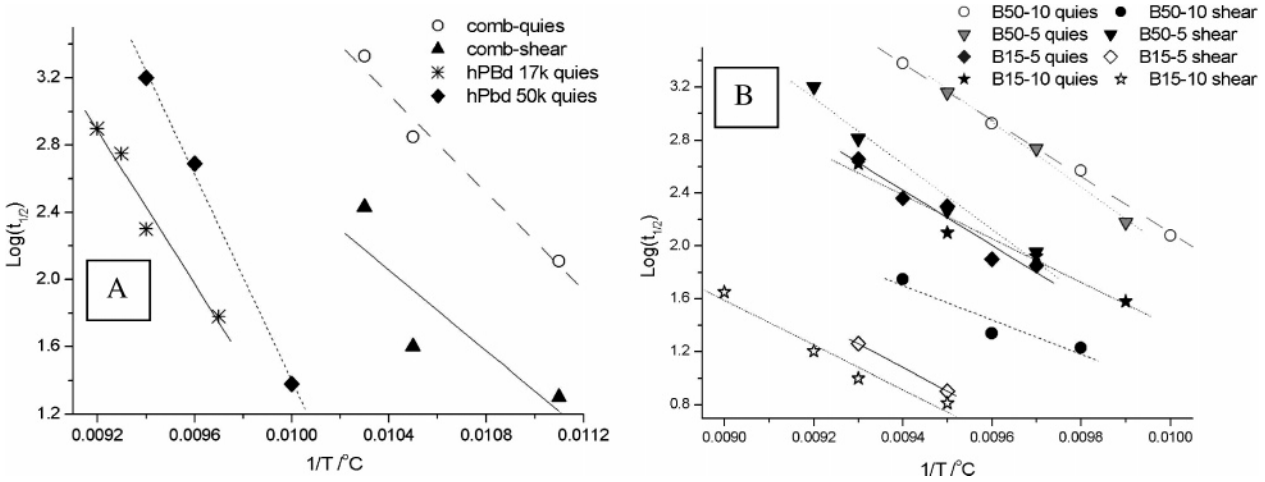

Figure 14. Crystallization half-times ($t_{1/2}$) for: (A) linear homopolymers and pure comb samples and (B) the blends. Lines give comparisons between shear-induced and quiescent crystallizations at several temperatures.

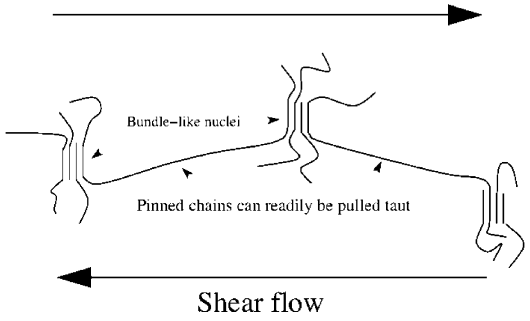

Figure 15. Possible mechanism for the formation of threadlike nuclei. Chain segments between nucleation events are pulled taut by the flow.

produce shish kebab structures and the subsequent oriented crystal growth, the large bond orientation resulting from strong stretching is required.[2] This implies that moderate stretching is sufficient to enhance crystal nucleation. Chain stretch relaxes with a time scale that is determined by the chain Rouse time, τ_R. We calculate these Rouse times for all materials in this study in Appendix A. To deduce the amount of stretching produced in a particular flow, one must compare the Rouse time to the deformation rate through the dimensionless Weissenberg number, which is the product of the deformation rate and relaxation time. In terms of the shear Weissenberg number, the condition for weak stretching is $\dot{\gamma}\tau_R > 1$, and for strong stretching, $\dot{\gamma}\tau_R \gg 1$ is necessary.[48] The precise quantitative condition for strong stretching, particularly in shear, is not well established. Recent work has demonstrated that the degree of chain stretching in steady shear increases slowly with shear rate for entangled polymers,[49] explaining why large Weissenberg numbers are necessary for strong stretching in shear. In the case of comb−linear blends, the comb stretching is controlled by the comb Rouse time, τ_R^{Comb}, which is mediated by the linear matrix. These time scales are computed in Appendix A.

The above argument, based on the shear rate compared to stretch relaxation times, does not explain the observation that oriented growth is very sensitive to the HM_w concentration. References, 7, 8, along with our data, demonstrate that oriented growth is sharply enhanced when the HM_w concentration exceeds c^*, suggesting that a cooperative effect between slowly relaxing chains controls the formation of shish. This observation can be explained by the hypothesis that nucleation points are able to act as effective cross links under flow, as shown in Figure 15. If a HM_w chain participates in two distinct nuclei, it will effectively be pinned in the bulk melt. Consequently, its relaxation will be severely impeded and the flow will readily pull the molecule taut. These taut molecules will form threadlike nuclei. For this to occur, nucleation sites must be sufficiently close together to allow molecules to participate in multiple nucleation events. In other words, the comb concentration must above the overlap concentration, c^*. The bundlelike nuclei shown in Figure 15 correspond to the very early stages of crystallization, and our hypothesis does not suggest that oriented lamellae are formed before the threadlike nuclei. Instead, we suggest that lamellae growth occurs later, around the oriented nucleation sites provided by the taut chains.

We computed the overlap concentration to be 6%, so that the 10% blends are sufficiently concentrated but the 5% comb blends are below this threshold. A further condition is that the flow-induced nucleation rate must be rapid enough to produce the required nucleation density during the flow. That is, even if the potential nucleation sites are sufficiently concentrated, if an insufficient fraction are activated by the flow, the creation of threadlike nuclei will be impossible. Although the dependence of the nucleation density on flow conditions is more difficult to estimate, the nucleation rate should increase as $\dot{\gamma}\tau_R^{Comb}$ increases, so there must be a critical Weissenberg number that produces the necessary nucleation density. It is meaningful to compare Weissenberg numbers across all of the blends in this study because all other shear conditions (e.g., total strain, shear geometry, etc.) are identical in all our experiments. This critical Weissenberg number may lower with increased concentration, although a direct theoretical connection between shear history and nucleation density cannot be made at this stage.

The above arguments are summarized in Figure 16, a nonequilibrium morphology map with Weissenberg number and comb concentration as the independent variables. The positions of all blend data points are known from the calculations in Appendix A. The multiple points corresponding to each blend arise from measurements at different temperatures, producing small changes in τ_R^{Comb}, computed by time−temperature superposition, as described in Appendix A. The two conditions for oriented crystals in the blends are plotted as dashed lines. The concentration condition can be readily plotted because c^* is known. However, the line corresponding to the critical Weissenberg number cannot be accurately positioned. Our only approach here is to use our experimental result that blend B50−10 shows oriented crystals, indicating that this line must bisect the points corresponding to blends B50−10 and B50−5, as drawn. A number of features arise from Figure 16. Our four-

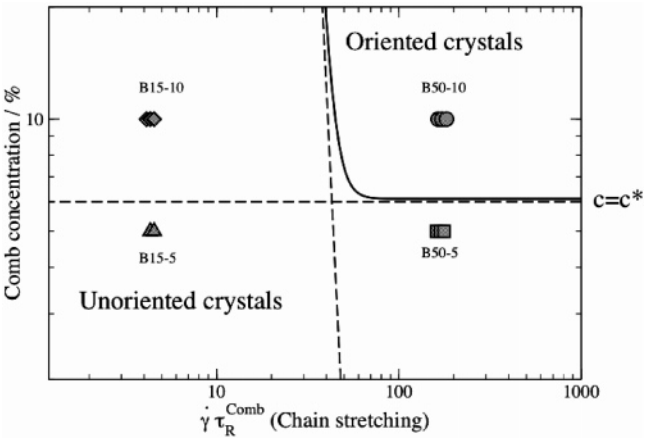

Figure 16. Nonequilibrium morphology map for crystal orientation as determined by comb concentration and shear Weissenberg number.

blend compositions appear to fall one into each of the four quadrants defined by the conditions for oriented crystals. Thus, in our data, both conditions must be met for oriented growth. Also, blend B50−5 falls just below *c**, yet despite its very high stretch Weissenberg number, there is no evidence of oriented crystals in the SAXS data from this material. This indicates that, with our monodisperse materials, the transition between isotropic and oriented crystals occurs quite sharply between 5 and 10%, which is around *c**. In summary, our proposed shish formation mechanism (Figure 15) directly explains the strong influence of high-molecular-weight concentration on final flow-induced morphology. In particular, it explains the change from spherulites to shish kebabs between blends B50−5 and B50−10 even though both blends are sheared with the same Weissenberg number. However, a direct microscopic confirmation of this mechanism is not possible using our experimental protocol, and further investigation is required to validate this picture.

6. Conclusions

We have performed a quantitative investigation of the effect of molecular structure on flow-induced crystallization. We investigated blends of monodisperse materials which, when combined with molecular theory, allow us to unambiguously define blending concentrations and component relaxation times. As our high-molecular-weight components are long-chain branched, a particularly wide separation of time scales between the components was achieved, which allowed us to isolate the influence of the HM_w fraction on flow-induced nucleation. Various regimes of deformation rate and concentration were identified and could be related to the orientation observed in the final crystal structure. We identified four regimes of flow rate and HM_w concentration and demonstrated at our four blends fall one into each regime. From our results, we presented a hypothesis to explain how molecular structure and flow conditions control the orientation of crystal morphology. This hypothesis can be tested by future experiments, investigating flow rates and concentrations that are intermediate to these results.

We have also discussed the connection between crystal growth kinetics and molecular configuration under flow. When the crystal growth remains isotropic, the crystallization half-time is inversely proportional to the comb density, suggesting that the comb dynamics are unaffected and that only the density of potential flow-induced nucleation sites changes. When considering the transition to threadlike nuclei, this qualitative change in kinetics induces a stronger dependence of the half-time on comb concentration. More detailed theories relating flow-induced crystallization to molecular motion are needed to obtain a deeper understanding into these results. In particular, a theoretical connection between molecular configuration and nucleation would allow a more quantitative interpretation of our data. Further factors, such as the effect of shear time and temperature, may also be influential and warrant investigation. Similar results may also be possible with linear−linear blends of monodisperse polymers.

Acknowledgment. E.L.H. and C.M.F. were supported from the EPSRC microscale polymer processing project (GR/M60415 and GR/T11807/01). The experimental X-ray beam time at the ESRF was provided under the LTP SC 777. We are grateful for the assistance of all the ESRF Dubble-CRG staff. We thank Alexei Likhtman for assistance with the time scale calculations.

Appendix A: Time Scale Calculations

The amount of deformation at a molecular level caused by flow is determined by comparing the molecular relaxation times to the shear rate. Thus, the relaxation times are essential for a meaningful comparison of flow-induced crystallization between different molecular weights, architectures, and chemistries. In this Appendix, we predict the various relaxation times for the samples in this study and then confirm these time scales by comparing to linear oscillatory shear measurements (see Section 3.2 for details of these measurements). These time scales are used in the main document when interpreting the crystallization data. The Doi−Edwards tube theory [10] is the most successful model for the dynamics of concentrated polymer fluids. In this approach, the complicated many-body interactions that arise because neighboring chains cannot pass through each other are modeled, in a mean-field way, as an effective tubelike constraint around the test chain. We employ three different models, all based around the tube theory,[10] to model the different architectures in this work. To model the pure linear polymers, we use the recent theory by Likhtman and McLeish,[50] for pure combs, we use the theory of Daniels et al.[51] as implemented by Inkson et al.,[52] and to model the comb−linear blends, we use a simple combination of these two theories.

Two primary relaxation mechanisms emerge from the tube model. Chains relax their orientation by diffusing back and forth along the tubes defined by the chain contour. This process is known as reptation and occurs on a time scale τ_d, the reptation time. A large deformation may also increase the contour length or stretch of a chain and this is relaxed by retraction. The chain retracts along its tube, driven by its entropic spring force, moving the stretch toward its equilibrium value with no change in orientation. The time scale for this mechanism is the chain Rouse time, τ_R. In all cases, $\tau_d > \tau_R$. The long-chain branching in the comb molecules significantly increases both τ_d and τ_R relative to the linear chains because the sidearms strongly impede the relaxation. In fact, the extra effective drag from the side branches increases exponentially with arm length.[51] All time scales can be computed from the chain architecture along with three molecular parameters, each of which depends on the chemical species but not molecular weight or topology. These parameters are the Rouse time of an entanglement segment, τ_e, the molecular weight between entanglements, M_e, and the plateau modulus, G_N^0. For hPBd, at 170 °C, these parameters are: $\tau_e = 11.9$ ns, $M_e = 1.26$ kg/mol^{-1}, and $G_N^0 = 2.25$ MPa.[53] The time scale τ_e was shifted to 170 °C using time−temperature superposition (TTS) with the WLF parameters: $C_1 = 1.80$, C_2

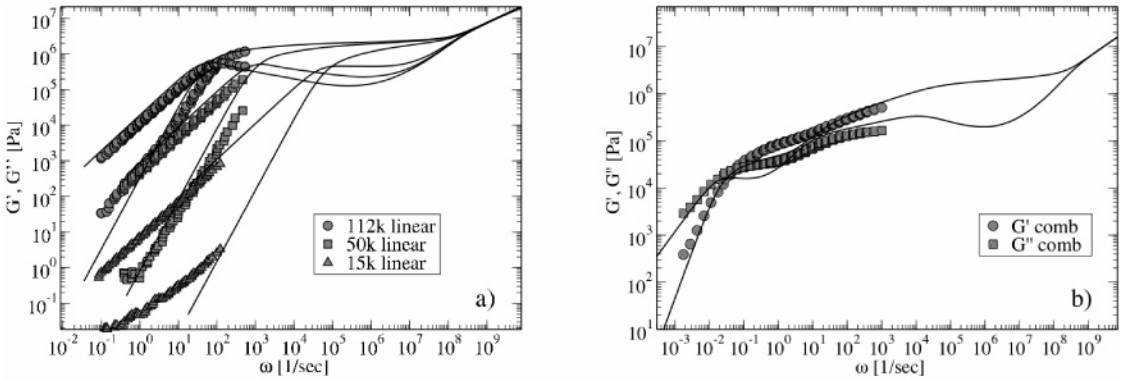

Figure 17. Comparison of linear shear rheology, at 170 °C: (a) pure linear samples with the Likhtman and McLeish theory,[50] (b) pure comb with the Daniels[51] and Inkson [52] theories.

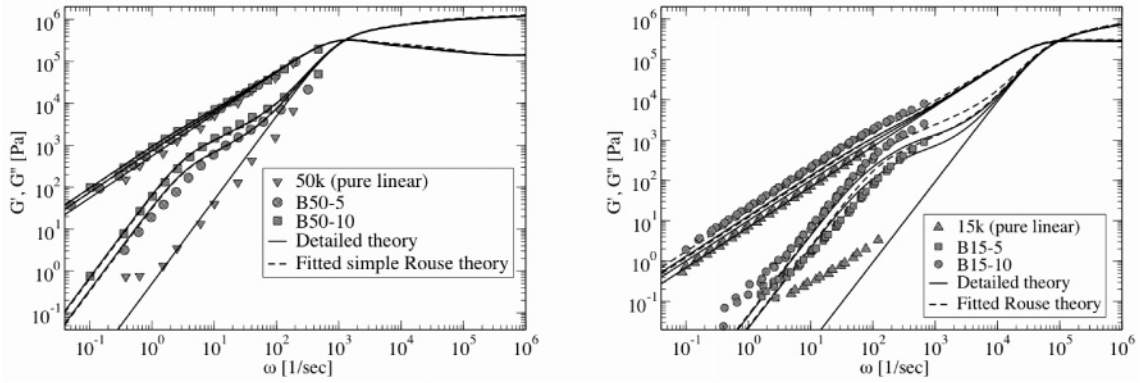

Figure 18. Linear rheology, at 170 °C, of comb linear blends compared with a detailed self-consistent theory and a simple Rouse theory where τ_R^{Comb} is taken as a free-fitting parameter.

$= 283$ K, and $T_{ref} = 170$ °C.[15] These literature values for the TTS parameters were found to superpose our frequency sweep data from a range of temperatures very well. The comparisons between theory and experimental data for the pure linears and the pure comb, using only these parameters, are shown in Figure 17. Given that good agreement between data and theory is found using only literature parameters, we conclude that the molecular theories are reliable and that they provide accurate values for the molecular relaxation times.

Theories for comb−linear blends are not as well established as those for pure combs or linears. In this case, we make a relatively simple generalization of the linear and comb theory used above. For all of our comb−linear blends, the combs are self-dilute and so no comb−comb entanglement effects are observed. Furthermore, the normal reptation and retraction processes of the combs are significantly hindered by the branch points. In this situation, the fastest relaxation mechanism for the comb backbone is via the release of constraints due to linear chains. Under the action of constraint release, the entangled comb behaves like a free Rouse chain with segment mobilities set by the motion of the linear chains. We denote the longest relaxation time for this process τ_R^{Comb} which, at a scaling level, can be estimated as:

$$\tau_R^{Comb} \approx c_\nu s_b^2 \tau_d^{linear} \tag{6}$$

where s_b is the number of entanglements along the comb backbone, τ_d^{linear} is the reptation time of the linear matrix, and c_ν is an order one parameter that controls the strength of constraint release (see refs 10, 50, and 51 for full details). A simple estimate for the comb contribution to the linear relaxation modulus is a Rouse spectrum.

Table 7. Relaxation Times for the Comb−Linear Blends at 106 °C[a]

time scale/s	15 K	50 K	pure comb
τ_e	4.00×10^{-8}	4.00×10^{-8}	4.00×10^{-8}
τ_d	2.4×10^{-4}	4.80×10^{-3}	154
τ_R	5.00×10^{-6}	6.30×10^{-5}	2.49
τ_R^{Comb}	0.044	1.65	N/A

[a] τ_d and τ_R refer to the linear materials and τ_R^{Comb} refers to the dilute comb. All time scales are independent of comb concentration at the concentrations used in this work.

$$G(t) = \phi_b G_N^0 \frac{1}{s_b} \sum_{i=1}^{s_b} \exp\left(\frac{-2t}{\tau_R^{Comb}}\right) \tag{7}$$

This contribution is proportional to comb concentration and is added to the spectrum of the linear matrix. Equation 7 corresponds to assuming that each entanglement segment of the comb has the same mobility, which is due to a single constraint release rate determined by the reptation time of the linear chains. However, in reality, the combs experience a broad spectrum of relaxation times resulting from the range of relaxation processes available to the linear chains in the matrix. This can be accounted for self-consistently with the constraint release algorithm used in ref 50. This algorithm replaces the sum in eq 7 with a numerically computed series of Maxwell modes, which is determined from the dynamics of the linear matrix. The results of these calculations are shown in Figure 18. In both pairs of blends, the addition comb material produces an extended shoulder in the elastic modulus, the size of which is proportional to the comb concentration. This confirms that, as expected from

the c^* calculations, the comb dynamics are independent of concentration and that, when the matrix material is fixed, the pairs of blends have identical comb relaxation times. To capture the comb contribution quantitatively, we required a separate value of the constraint release parameter, c_v, for each matrix length. We used $c_v = 0.4$ for blends B50−10 and B50−5 and 1.0 for blends B15−10 and B15−5. Although these values are within normal limits, there is scope for further theoretical progress in understanding comb−linear blends.

Also included in Figure 18 is the simple Rouse theory of eq 7, where τ_R^{Comb} is taken as a fitting parameter, which does not change with comb concentration. The resulting time scales for the linear and comb samples are summarized in Table 7. Under nonlinear response, τ_R^{Comb} will control the relaxation of both stretch and orientation of the combs in the comb−linear blends.

References and Notes

(1) Ward, I. M. *Structure and Properties of Oriented Polymers*; Wiley: New York, 1975.
(2) Keller, A.; Kolnaar, H. W. *Flow Induced Orientation and Structure Formation In Processing of Polymers*; Meijer, H. E. H., Ed.; VCH: New York, 1997; p 189.
(3) Stadlbauer, M.; Janeschitz-Kriegl, H.; Eder, G.; Ratajski, E. *J. Rheol.* **2004**, *48*, 631.
(4) Kornfiled, J. A.; Kumaraswamy, G.; Issaian, A. M. *Ind. Eng. Chem. Res.* **2002**, *41*, 6383.
(5) Kumaraswamy, G.; Kornfield, J. A.; Yeh, F.; Hsiao, B. S. *Macromolecules* **2002**, *35*, 1762.
(6) Kumaraswamy, G.; Verma, R. K.; Kornfield, J. A.; Yeh, F.; Hsiao, B. S. *Macromolecules* **2004**, *37*, 9005.
(7) Seki, M.; Thurman, D. W.; Oberhauser, J. P.; Kornfield, J. A. *Macromolecules* **2002**, *35*, 2583.
(8) Yang, L.; Somani, R. H.; Sics, I.; Hsiao, B. S.; Kolb, R.; Fruitwala, H.; Ong, C. *Macromolecules* **2004**, *37*, 4845.
(9) Crist, B.; Tanzer, J. D.; Graessley, W. W. *J. Polym. Sci., Part B: Polym. Phys.* **1987**, *25*, 545.
(10) Doi, M.; Edwards, S. F. *The Theory of Polymer Dynamics*; Oxford University Press: Oxford, 1986.
(11) Fernyhough, C. M.; Young, R. N.; Poche, D.; Degroot, A. W.; Bosscher, F. *Macromolecules* **2001**, *34*, 7034.
(12) Gedde, U. L. F. *Polymer Physics*; Chapman & Hall: London, 1995.
(13) Krigas, T. M.; Carella, J. M.; Struglinski, M. J.; Crist, B.; Graessley, W. W. *J. Polym. Sci., Polym. Phys. Ed.* **1985**, *23*, 509.
(14) Defoor, F.; Groeninckx, G.; Reynaers, H.; Schouterden, P.; Van de Heijden, B. *Macromolecules* **1993**, *26*, 2575.
(15) Pearson, D. S.; Fetters, L. J.; Graessley, W. W.; Strate, G. V.; Vonmeerwall, E. *Macromolecules* **1994**, *27*, 711.
(16) Bras, W.; *J. Macromol. Sci., Phys.* **1998**, *B37*, 557.
(17) Ryan, A. J. *J. Therm. Anal.* **1993**, *40*, 887.
(18) Bras, W.; Derbyshire, G. E.; Mant, G. R.; Clarke, S. M.; Cooke, J.; Komanschek, B. U.; Ryan, A. J. *J. Appl. Crystallogr.* **1994**, *28*, 26.
(19) Somani, R. H.; Hsiao, B. S.; Nogales, A.; Srinivas, S.; Tsou, A. H.; Sics, I.; Balta-Calleja, F. J.; Ezquerra, T. A. *Macromolecules* **2000**, *33*, 9385.
(20) Li, L.; de Jeu, W. H. *Macromolecules* **2003**, *36*, 4862.
(21) http://www.dl.ac.uk/SRS/NCD.
(22) Heeley, E. L.; Maidens, A.; Olmsted, P. D.; Bras, W.; Dolbnya, I. P.; Fairclough, J. P. A.; Terrill, N. J. Ryan, A. J. *Macromolecules* **2003**, *36*, 3656.
(23) Vonk. C. G.; Kortleve, G. *Kolloid Z. Z. Polym.* **1969**, *220*, 19.
(24) Alexander, L. E. *X-ray Diffraction Methods in Polymer Science*; Wiley: New York, 1969.
(25) Glatter, O.; Kratky, O. *Small-Angle X-ray Scattering*; Academic Press Inc.: London, 1982.
(26) Avrami, M. *J. Chem. Phys.* **1939**, 7, 1103; **1940**, *8*, 212.
(27) Schultz, J. M. *Polymer Crystallization: The Development of Crystalline Order in Thermoplastic Polymers*; Oxford: New York, 2001, pp 182−183.
(28) Sharples, A. *Introduction to Polymer Crystallization*; Edward Arnold Ltd.: London, 1966.
(29) Strobl, G. R.; Engelkek, T.; Maderek, E.; Urban, G. *Polymer* **1983**, *24*, 1585.
(30) Maderek, E.; Strobl, G. R. *Colloid Polym. Sci.* **1983**, *261*, 471.
(31) Baltá-Calleja, F. J.; Vonk, G. G. *X-ray Scattering of Synthetic Polymers*; Elsevier Science: New York, **1989**.
(32) Strobl, G. R.; Schneider, M. *J. Polym. Sci., Polym. Phys. Ed.* **1980**, *18*, 1343.
(33) Strobl, G. R.; Schneider, M.; Voigt-Martin, I. G. *J. Polym. Sci., Polym. Phys. Ed.* **1980**, *18*, 1361.
(34) Porod. G. *Kolloid-Z.* **1951**, *124*, 83.
(35) Ryan, A. J. *Fibre Diffr. Rev.* **1994**, *3*, 25.
(36) http://www.ccp13.ac.uk/software/software.htm.
(37) Rober S.; Bosecke, P.; Zachmann, H. G. *Makromol. Chem., Macromol. Symp.* **1988**, *15*, 295.
(38) Ryan, A. J.; Hamley, I. W.; Bras, W.; Bates, F. S. *Macromolecules* **1995**, *28*, 3860.
(39) Hamley, I. W.; Fairclough, J. P. A.; Bates, F. S.; Ryan A. J. *Polymer* **1998,** *39*, 1429.
(40) Statton, W. O. *J. Appl. Phys.* **1961**, *32*, 2332.
(41) Boyd, R. H. *Polymer* **1985**, *26*, 1123.
(42) Peeters, M.; Goderis, B.; Vonk, C.; Reynaers, H.; Mathot, V. *J. Polym. Sci., Part B: Polym. Phys.* **1997**, *35*, 2689.
(43) Crist, B.; Howard, P. R. *Macromolecules* **1999**, *32*, 3057.
(44) Crist, B.; Williams, D. N. *J. Macromol. Sci., Phys.* **2000**, *B39*, 1.
(45) Stribeck, N. *Colloid Polym. Sci.* **1989**, *267*, 301; **1992**, *270*, 9.
(46) Stribeck, N.; Apostolov, A. A.; Zachmann, H. G.; Fakirov, C.; Stamm, M.; Fakirov, S. *Int. J. Polym. Mater.* **1994**, *25*, 185.
(47) Göschel, U.; Urban, G. *Polymer* **1995**, *36*, 3633.
(48) Elmoumni, A.; Winter, H. H.; Waddon, A. J. *Macromolecules* **2003**, *36*, 6453.
(49) Graham, R. S.; Likhtman, A. E.; McLeish, T. C. B.; Milner, S. T. *J. Rheol.* **2003**, *47*, 1171.
(50) Likhtman, A. E.; McLeish, T. C. B. *Macromolecules* **2002**, *35*, 6332.
(51) Daniels, D. R.; McLeish, T. C. B.; Kant, R.; Crosby, B. J.; Young, R. N.; Pryke, A.; Allgaier, J.; Groves, D. J.; Hawkins, R. J. *Rheol. Acta* **2001**, *40*, 403.
(52) Inkson, N. J.; Graham, R. S.; McLeish, T. C. B.; Groves, D. J.; Fernyhough, C.; *Macromolecules* **2006**, *39*, 4217.
(53) Likhtman, A. E. *Macromolecules* **2005**, *38*, 6128.

MA0606307